Effects of Cation Disorder on Oxygen Vacancy Migration in Gd$_2$Ti$_2$O$_7$

R.E. WILLIFORD, W.J. WEBER & R. DEVANATHAN

Materials Department, Pacific Northwest National Laboratory, Richland, WA 99352

J.D. GALE

Department of Chemistry, Imperial College, South Kensington, London, UK SW7 2AY

Abstract. Atomistic simulations were used to calculate defect formation and migration energies for oxygen vacancies in the pyrochlore Gd$_2$Ti$_2$O$_7$, with particular attention to the role of cation antisite disorder. Oxygen occupies two crystallographically distinct sites (48f and 8a) in the ordered material, but the 8b sites become partially occupied with disorder. Because cation and anion disorder are coupled, oxygen vacancy formation and migration energetics are sensitive to the configuration of the cation disorder. The V$_{O48f}$ vacancy and V$_{O48f}$ + O8b$_i$ Frenkel defects are energetically favored in the ordered material, but V$_{O8a}$ is favored at higher disorder. The V$_{O8a}$ + O8b$_i$ Frenkel is favored for some disorder configurations. Eight possible oxygen vacancy migration paths converge toward a unique migration energy as cation disorder increases, reflecting a reversion towards the fluorite structure. Oxygen vacancy migration is determined by O$_{48f} \rightarrow$ O$_{48f}$ transitions along the shortest edges of the TiO$_6$ octahedra. The transition V$_{O8a} \rightarrow$ V$_{O48f}$ is also possible for low disorder, and can activate the V$_{O48f} \rightarrow$ V$_{O48f}$ migration network by depositing vacancies there. The reverse transition may occur at very high disorder to retard ionic conduction, and is consistent with Frenkel defect stabilities. Local regions of ordered and disordered material both appear necessary to explain the observed trends in ionic conductivity.

Keywords: Gd$_2$Ti$_2$O$_7$, pyrochlores, disorder, oxygen vacancy migration

1. Introduction

Solid oxide electrolytes are advantageous high-temperature materials for the active elements in fuel cells, oxygen sensors, and ion pumps [1], to name a few applications. One system of interest is the Gd$_2$(Zr$_x$Ti$_{1-x}$)$_2$O$_7$ pyrochlores, or GZT in abbreviated form. This system has been extensively studied by Tuller, et al., [2] because of its intrinsic fast oxygen ion conductivity and the possibility of lower temperature operation compared to other materials such as ZrO$_2$. The lattice parameter can also be controlled by the Zr content, which can be very useful for minimizing substrate/lattice strains for thin film applications. GZT offers a flexible cation chemistry that may be adjusted to suit the requirements of a

particular application [1]. In addition, Gd$_2$Ti$_2$O$_7$ and related pyrochlore materials are potential phases for the immobilization of actinides in nuclear waste and plutonium from the weapons program [3]. Consequently, radiation effects (cation disorder) on defect mobility are of great interest.

Extensive experimental work [1,2,4,5] has shown that the substitution of Zr for Ti is associated with a large increase in ionic conductivity due to an increase in the carrier concentration, while electronic conductivity decreases. The onset of these conductivity changes is at about $x = 0.25$, and saturation is approached at about $x = 0.6$. Oxygen vacancies have been shown to be the dominant migrating species, with an activation energy of about 1.0–1.2 eV at low temperatures (0.8 eV for temperatures

above about 800°C). The increase in ionic conductivity is associated with cation antisite disorder, which has been verified by X-ray [5] and neutron diffraction [6] experiments. Very small amounts of disorder are caused by entropic effects at $x = 0$. Cation antisite disorder has been estimated [5] to be $< 5\%$ at $x = 0.25$. At $x = 0.6$, it is about 10%, and is associated with about 2% anion disorder in the form of Frenkel defects. The cation and anion disorder rise to about 35% and 5% at $x = 1.0$, where defect clustering causes the migration activation energy to increase. As x increases, GZT gradually reverts from the pyrochlore to a more fluorite-type structure, with a randomized ordering of the cations, along with partial emptying/filling of some oxygen sites that are normally filled/empty in the pyrochlore. More detail can be found in [1,2,4–6].

Because the disorder that enhances the ionic conductivity of GZT is not global, it must occur on a localized basis. The defect clustering that retards conductivity at high Zr content is also a localized phenomenon. Unfortunately, there exist no means to directly measure, on the localized scale of several atoms, how such specific *local* disorder affects the vacancy migration energetics. It is therefore advantageous to employ atomistic computer simulations for this purpose.

There have been two computer simulation studies of oxygen vacancy migration in these materials. Both used atomistic models with empirical pair potentials. Van Dijk, et al., [7] addressed ordered $Gd_2Zr_2O_7$. Wilde and Catlow's earlier work [8] studied both $Gd_2Ti_2O_7$ and $Gd_2Zr_2O_7$, also in the ordered state, while their more recent work addressed cation disorder using energy minimization [9] and molecular dynamics [10]. Both groups treated atomic polarization using shell models and a single set of interatomic potentials. The results below will indicate some of the advantages (and disadvantages) in using several sets of potentials so that comparisons can be made and trends in the dominant transport mechanisms identified. In the present work, the $x = 0$ end member of the GZT composition range is addressed. The $x = 1$ end member and other intermediate compositions were addressed in other publications [11].

Computer simulation of fundamental oxygen vacancy migration processes is the main objective of this paper. In the next section, the crystal structure of ordered $Gd_2Ti_2O_7$ is briefly outlined. This is followed by a description of the computational tools employed to simulate oxygen vacancy migration in this pyrochlore. The energetics of oxygen vacancy formation and migration are then calculated using three sets of empirical potentials and energy minimization techniques. The final section briefly discusses some of the uncertainties inherent in this approach, and summarizes the conclusions.

2. Pyrochlore Crystal Structure

The crystal structure of pyrochlores ($A_2B_2O_7$, or $A_2B_2O_6O'$) has been previously described in detail [12–17], and will only be briefly reviewed here. The space group is Fd3m, and there are 88 atoms in the complete cubic unit cell. Given the space group, just two more parameters are necessary to specify the entire structure: the cell size and the x position of the O atoms in the 48f positions. Several geometric approaches have been used for descriptions of the structure. One considers the structure as an ordered defect fluorite, with systematically vacant 8b sites. Another considers the pyrochlore as a set of interpenetrating B_2O_6 and A_2O' networks. The A_2O' forms zig-zag chains that pass through the centers of B_2O_6 hexagons, which in turn have the chair conformation. A diagram of this interpetration appears in [16]. For the present discussion of vacancy migration paths, the polyhedral representation [18] seems useful, as follows.

Each B atom is coordinated with six oxygens, forming slightly distorted octahedra with edges of two lengths: for $Gd_2Ti_2O_7$, these lengths are 0.265 and 0.285 nm, as shown in Fig. 1. These octahedra fit together in what has been called the basic pyrochlore structural unit: four corner-sharing octahedra with a
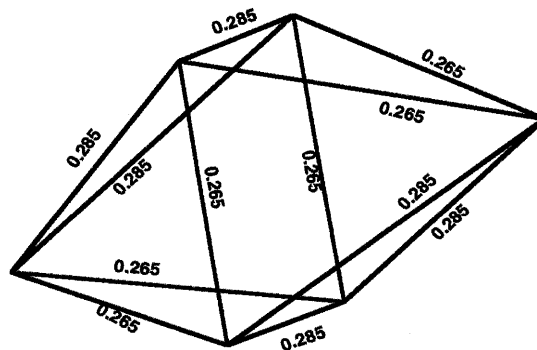

Fig. 1. The basic BO_6 octahedron for $Gd_2Ti_2O_7$, with edge lengths shown in nm. The central B atom is not shown for clarity.

central octahedral void, as in Fig. 2. These groups of four octahedra can be viewed as being arranged about rows of A atoms, as in Fig. 3, which also shows the positions of the oxygens in the 8a positions within the central hexagonal channels containing the A rows. The 48f oxygens occupy the corners of the octahedra. The A (Gd) atoms which appear in this figure to be embedded in the octahedra are actually members of other A rows which intersect those shown. There are three distinct oxygen sites: the 48f is coordinated by two Gd and two Ti, the 8a (normally occupied in pyrochlores) is coordinated by four Gd, and the 8b (normally unoccupied in pyrochlores) is coordinated by four Ti atoms.

3. Computational Methods

Static lattice energy minimization techniques are justified by the strongly ionic nature of $Gd_2Ti_2O_7$. The General Utility Lattice Program (GULP) [19,20] was used in this investigation to simulate the energetics and structures of perfect lattices and of

Fig. 2. The basic pyrochlore structural unit: four corner-sharing BO_6 octahedra.

defects. GULP includes the facility for energy minimization based on the Born model, where energy is partitioned into long ranged Coulombic interactions computed via the Ewald summation technique, and short ranged atomic pairwise or three-body interactions. The code is unique in that it optimizes the use of crystal symmetry to make structure generation easier and to speed up calculations through the symmetrization of the energy components and its derivatives up to second order.

Isolated defects in extended solids were addressed using the Mott-Littleton approximation [21]. In this well-known method, the crystal surrounding the defect is divided into three spherical regions of progressively larger radii. Region 1 contains the defect *per se,* where interactions are treated explicitly at the atomic level and ions are relaxed in response to all components of the force due to the defect. In Region 2a, the ions are assumed to reside in a harmonic well and respond accordingly to the electrostatic component of the defect forces. This approximation is only valid for small perturbations in Region 2a (i.e., Region 1 must be of sufficiently large radius) and requires that the bulk lattice be relaxed prior to introduction of the defect (a standard procedure). Individual ion displacements are still treated in Region 2a, whereas only the implicit polarization of sublattices due to the total defect charge is considered in Region 2b. A defect formation energy is calculated as the energy difference between the defective (E_{def}) and perfect (E_{perf}) lattices, and corrected for the energy of interstitials or vacancies at
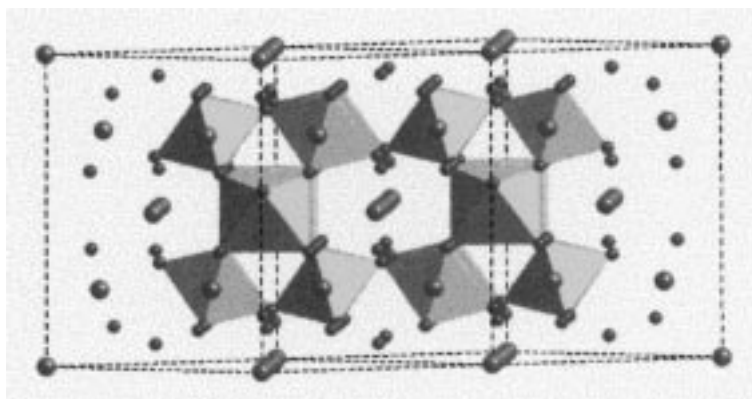
Fig. 3. Polyhedral representation of the pyrochlore structure, showing BO_6 octahedra in a $2 \times 1 \times 1$ supercell along the $\langle 110 \rangle$ axis. B (Ti or Zr) atoms are not shown for clarity. The small spheres at each octahedron corner are the 48f oxygen atoms. The larger isolated spheres are A (Gd) atoms. The small isolated spheres above and below the A rows are oxygen atoms in the 8a positions. The 8b positions are above and below the 8a positions, in the interstices between the BO_6 octahedra.

infinite separation from the lattice: $E_{\mathrm{defect}} = E_{\mathrm{def}} - E_{\mathrm{perf}} + E_{\mathrm{inf}}$. The GULP code calculates defect energies, rather than reaction enthalpies. $E_{inf} = 0$ since the empirical potentials used here are defined with respect to zero energy at infinity. Further details of the computational method are given elsewhere, e.g., [22].

Charged defects polarize other ions in the lattice. Ionic polarization was treated using the well-known Dick-Overhauser shell model [23] and includes the important coupling between short range repulsion and ion polarization, which prevents excessive polarization from occuring. A simple harmonic spring model is often used to represent the separation of the electron cloud from the ionic core. Within an ion, the shell charge and spring constant combine to determine the overall electronic polarizability. The net ionic (core + shell) charge may depart from formal charges in order to approximate the effects of partial covalency.

An important capability of GULP for the present work was the ability to perform transition state searches using a rational function optimizer, where an energetic ''saddle point'' was found by seeking atomic positions with a specified number of imaginary eigenvalues in the Hessian [19]. Thus, calculations of the activation energies for vacancy migrations could be routinely performed in two steps. In the first step, the defect energy of a single vacancy was calculated as described above, using standard energy minimization techniques. In the second step, an interstitial was placed between the two vacancies which were the initial and final positions of the migrating ion corresponding to the migrating vacancy, and a transition state with one imaginary eigenvalue was sought. After a transition state was found, the migrating ion was then displaced from this saddle point position and its energy minimized to check for the correct minima on either side of the transition state. The difference between the defect energies of these two calculations gave the activation energy for vacancy migration. The results of such calculations are described below.

4.   Interatomic Potentials for Pyrochlores

Three sets of potentials were employed for comparative purposes: (1) the Wilde and Catlow (W&C) set of potentials [8,9], (2) the potential set by Bush et al. [24]

and (3) a third set derived specifically for this work. Each potential set is described below.

The Wilde and Catlow potentials [8,9] were first developed in 1991 for studying the same pyrochlores of the present paper. They incorporated Catlow's well-known O-O potential derived by Hartree-Fock methods [25]. Wilde and Catlow used the THBREL code to simulate perfect lattices, and the CASCADE code to simulate defects. Results for these potentials are described in later sections.

The potential set by Bush, et. al. [24] was developed in 1994 to simultaneously match the structures, elastic constants, and dielectric constants of 22 binary oxides. They obtained a truly empirical O-O potential by allowing it to be fitted without constraints, and obtained a dispersion term for the resulting Buckingham-type potential which was in good agreement with the quantum-mechanical value for MgO [26]. The Bush potentials gave reasonable structures and elastic constants for $Gd_2Ti_2O_7$, but the static dielectric constant was predicted to be negative, which is not physically realistic. Imaginary phonon modes were also present, indicating that the structure tends to distort to a lower symmetry than allowed within the experimental space group. When this is permitted, the distortions are small and thus we have worked within the constraint of the higher symmetry. These imaginary modes were partly responsible for code convergence problems when cation disorder was addressed. Another source of this problem originated from the Ti shell model, which was derived for rutile TiO_2 to match its high dielectric constant, and which historically gives stability problems when applied to lower symmetry structures. Attempts to refit the Bush potentials with a rigid Ti ion model were unsuccessful. Consequently, some of the calculations desribed below are incomplete.

As indicated above, a stable structure with no imaginary phonon modes is a necessary first step for energy minimization calculations. An unstable structure will often relax during energy minimization, especially when symmetry is broken by the presence of a defect, thus contributing anomolous relaxation energies to the defect energy. Beyond this, the curvature properties of the potentials are also very important, since they determine the physical constants of the material through derivatives [19]. While the above instabilities were not evident in the W&C potentials, they used a Ti shell model with a very large shell charge (-35.8 |e|) and harmonic spring constant

(65974.0 eV/Å^6), neither of which seemed physically reasonable for the present system. The third set of potentials was developed to alleviate these difficulties, as follows. First, the Ti shell was eliminated, and a new rigid-ion Ti-O potential was developed by ''relaxed fitting'' [20] to the rutile TiO$_2$ structure and physical properties, for which results were good (i.e., a volume change of only 0.64% when fitted at constant pressure, and a static dielectric constant of 64.2). Then using the Catlow O-O potential [25] and the Lewis and Catlow Gd-O potential [8,9,27], new oxygen shell parameters were found as follows.

It is known that anion polarizability is strongly dependent on the local crystal environment [27,28]. The O48f and O8a atoms were therefore treated as distinct species in a second stage of ''relaxed fitting'' [20] to the Gd$_2$Ti$_2$O$_7$ structure and elastic and dielectric constants. This is reasonable since the O48f has two Gd and two Ti as near neighbors (total cationic charge of $+14$), while the O8a has four Gd near neighbors (total cationic charge of $+12$). Furthermore, each Gd is eight-coordinated with oxygens, while each Ti is only six-coordinated, which maintains a higher cationic charge for the O48f atoms. Consequently, the O48f should have a higher polarization than the O8a. This is reflected in the ratio of polarizabilities (α = shell charge squared over spring constant) in Table 1: α(O48f)/α(O8a) = 2.64. This method was found preferable to introducing a large r^4 term in the harmonic core-shell spring constant [19], since the latter did not provide enough change in polarization to match the structures and properties. This approach of treating distinct oxygen sites as distinct species has also been used for structural models of other materials [29]. Parameters for the new potentials are shown in Table 1. For lack

of a better name, this model is called the ''distinct oxygen model,'' and abbreviated as DOM in this paper.

Some basic properties calculated for the materials using each of the three potential sets are shown in Table 2. The 48f x parameter is given for the ion cores. These numbers are slightly low compared to the more recent pyrochlore data base assembled in [14], which shows a 48f x parameter of 0.322 for Gd$_2$Ti$_2$O$_7$. However, they are in agreement with the earlier data [8] used to develop the W&C potential set, and with standard crystallographic data bases. The Bush potential set also gives agreement with the earlier data. Data for the unit cell dimensions are bounded by the predictions, with closest agreement given by the third set of potentials. Elastic constants (c_{ij}) are in reasonable agreement between the potentials, and the static dielectric constant (ε_{11}) is near the 50–60 range reported for these pyrochlores [7,8,13,30]. These potentials were used to calculate the basic defect formation energies shown in the next section.

5. Defect Formation Energies for the Ordered Material

Calculations for the W&C and Bush potentials used 100–120 ion cores in Region 1 for computational expediency, while calculations with the DOM potentials were performed with 300–315 ion cores for greater accuracy. Short range potential cutoffs were 1.2 nm for O–O and 1.0 nm for cation-O in the present work. Predictions of the basic defect formation energies are shown in Table 3, without defect charges for ease of notation. Results for the W&C potentials agree very well with their [8,9]

Table 1. Parameters for the DOM potentials. Potentials are all of the Buckingham form, and core-shell spring constants are harmonic. All cutoff distances were 1.0 nm, except 1.2 nm for O-O

Ions	A, eV	ρ, Å	C, eVÅ^6
O-O	22764.3	0.1490	27.89
Gd-O	1336.8	0.3551	0.00
Ti-O	740.0	0.3999	0.00

Ion	Core Charge (|e|)	Shell Charge (|e|)	Spring Constant (eVÅ^2)
Ti	4.2781	—	—
Gd	3.2500	-0.2500	145.00
O48f	0.6629	-2.7690	104.64
O8a	-0.0740	-1.8453	114.55

Table 2. Results for $Gd_2Ti_2O_7$ using three sets of potentials. Cell size is in nm, volume of the primitive cell is in nm^3, energies are in eV, and elastic constants are in GPa

Result	W&C	Bush	DOM	Experiment
lattice energy	− 711.61	− 749.36	− 783.02	—
O(48f) x param.	0.2982	0.3004	0.2996	0.3013
volume (prim.)	0.2751	0.2356	0.2676	0.2638
cell size (a,b,c)	1.0324	1.0047	1.023	1.0180
c_{11}	360.7	443.9	388.6	—
c_{12}	127.8	170.2	148.3	—
c_{44}	77.0	70.0	71.0	—
ϵ_{11}	41.15	− 91.48	39.13	60.0

Table 3. Defect formation energies for ordered $Gd_2Ti_2O_7$ using three sets of potentials. All energies are in eV/ defect. Frenkel energies (for isolated point defects) were calculated using the vacancy specie in the interstitial. The ''split vacancy'' case is a separate calculation, not the addition of elemental defect energies, using the O48f specie properties for the interstitial

Defect	W&C	Bush	DOM
V_{O48f}	17.06	13.75	19.10
V_{O8a}	20.52	18.88	18.92
$O8b_{i48f}/O8b_{i8a}$	− 11.42	− 9.54	−12.89/ − 8.72
Frenkel $V_{O48f} + O8b_i$	2.82	2.10	3.11
Frenkel $V_{O8a} + O8b_i$	4.55	4.67	5.10
Split Vacancy ($2V_{O48f} + O_i$)	5.72	4.92	6.66

calculations of $V_{O48f} = 16.96\,eV$, $V_{O8a} = 20.47\,eV$, and $O8b_i = -11.64\,eV$, despite their smaller potential cutoff distances (0.55 nm). Note that the W&C and Bush potentials both predict that the V_{O48f} formation energy is less than that for the V_{O8a}, while the reverse is true for the DOM potentials. The latter result seems more reasonable when the cationic charge around each site is considered, as above: the larger vacancy formation energy should occur for the anion surrounded by the larger cationic charge.

The oxygen interstitial in the 8b site is systematically vacant in ordered pyrochlores, but partially occupied in fluorites. The two entries in Table 3 for $O8b_i$ under ''DOM'' show the results of using the O48f versus the O8a shell properties for that interstitial, respectively. It appears that the W&C potentials are dominated by the O48f properties and the Bush potentials are dominated by the O8b properties, while the DOM potentials incorporate both.

From the above basic defect energies, the energetics of more complex defects can be calculated. In the following, each oxygen interstitial was calculated using the same short range potential along with the shell properties of the associated vacancy (see Table 2). Table 3 shows that an anion Frenkel defect composed of an isolated O48f vacancy and an isolated O8b interstitial would have the lowest energy in the ordered material. This result is in agreement with the conclusions of Wilde and Catlow [8,9] and Moon and Tuller [5]. Note that this is only valid for isolated (widely separated) vacancies and interstitials. Frenkel defects formed with first and second near neighbor vacancies and interstitials are discussed in a later section.

Also of interest is the O48f split vacancy discussed by van Dijk, et. al., [7] for $Gd_2Zr_2O_7$. This split vacancy has the O interstitial situated between two vacant O48f sites along a 0.285 nm TiO_6 $\langle 110 \rangle$ octahedron edge, and near an empty 8b site. They calculated that this configuration was favored by a formation energy 0.2 eV less than that for a simple O48f vacancy. Similar calculations were performed for $Gd_2Ti_2O_7$ in the present work. The O48f shell properties were used for the migrating atom with the DOM potentials. In Table 3, the energies are on a per defect basis, with two vacancies and one interstitial counted for the split vacancy, so the total energies for the split vacancy cases were 17.16, 14.76, and 19.98 eV for the W&C, Bush, and DOM potentials, respectively. It appears that the split vacancy is not favored for $Gd_2Ti_2O_7$, but only by a small amount for the W&C potentials.

6. Defect Formation Energies with Cation Antisite Disorder

This section treats the intrinsic, entropy-driven disorder in ideal $Gd_2Ti_2O_7$. Such disorder can also be caused by ion bombardment during ion beam experiments or in a nuclear waste isolation environment [3]. Unless otherwise stated, the configuration of the cation antisite disorder employed in this section is termed ''compact,'' as opposed to the ''open'' disorder treated elsewhere [11] and in later sections. ''Compact'' disorder is localized around the vacancy or interstitial site being treated. For example, the 48f site is coordinated by two Gd and two Ti at distances of 0.19 and 0.25 nm, respectively. This allows switching of the Gd and Ti atoms to form a compact cluster of disorder, as in [9]. ''Open'' disorder [11] uses the same Ti atoms, but these are switched with either one or two Gd atoms at greater distances, e.g., 0.47 nm from the 48f site.

The computational approach used most often for energy minimization is to treat the cation disorder as defects along with the oxygen vacancies and interstitials, so that the energy of all defects is computed simultaneously. A corrected vacancy or interstitial formation energy then requires that the energy of disorder alone be subtracted from the energy of point defect formation energy with disorder present. Table 4 shows formation energies for cation antisite disorder in the compact configuration with no vacancies or interstitials present. The notations 1X and 2X denote one pair and two pairs of switched Gd and Ti atoms, respectively. The Bush potentials did not converge for 2X compact disorder, illustrating the variation in results that can be obtained by using different sets of potentials.

Tables 5 and 6 show the predicted defect formation energies for 1X and 2X disorder, respectively. Each elementary defect (V_{O48f}, V_{O8a}, $O8b_i$) was corrected for the energy of cation antisite disorder from Table 4. The two entries for the 8b interstitial under ''DOM'' again depict the use of 48f and 8a shell properties in the interstitial, respectively. The Frenkel energies were computed from the elementary defect energies, and thus again represent isolated (widely separated) vacancies and interstitials. The 48f shell properties were used for the interstitial in the split vacancy case, which did not converge for the W&C potentials, presumably due to the Ti shell parameters. The higher energies of the split vacancies indicate that they are not preferred.

Although the scatter between potentials in Tables 5 and 6 makes it difficult to draw conclusions, averaging the results seems to clarify this situation somewhat, as shown in Fig. 4. The Frenkel and split vacancy energies are plotted here as total energies, for comparison to the elementary defect energies. The first ($V_{O48f} + O8b_i$) and second ($V_{O8a} + O8b_i$) Frenkels from Tables 3, 5 and 6 are denoted F1 and F2, respectively, for brevity of notation. For no cation antisite disorder, the V_{O48f} and F1 defects are preferred, as discussed above. For the 1X and 2X disorder cases, the O8a vacancy is energetically preferred. For 1X disorder, the two Frenkels have nearly the same energy, the second being only 0.04 eV/defect below the first. For 2X disorder, the F1 again appears preferred by 0.28 eV/defect. Results for only the DOM potentials (Fig. 5) are in agreement with the averages in Fig. 4, with the exception of a greater preference (0.37 eV/defect) for the F2 at moderate (1X) disorder.

7. Stability of Frenkel Defects

Experimental measurements show that the maximum in ionic conductivity occurs for a Zr content of about 60%, with a cation disorder of about 10%. It is thus reasonable to expect that this small fraction of disordered cation pairs will be rather dispersed within the material. This means that the disorder can be viewed as ''localized''. Experimental observations also show that cation and anion disorder occur simultaneously in these pyrochlores. Since the

Table 4. Cation antisite disorder energies (eV) for the compact configuration around the 48f site. The notation 1X indicates one disordered near neighbor pair ($Gd_{Ti} + Ti_{Gd}$), and 2X indicates two pairs

Disorder	W&C	Bush	DOM
1X	1.50	0.12	3.53
2X	6.11	—	7.33

Table 5. Defect formation energies (eV/defect), corrected for one pair of compact cation antisite defects. Frenkel energies are for isolated point defects

Defect	W&C	Bush	DOM
V_{O48f}	18.16	15.59	18.40
V_{O8a}	18.28	15.93	13.53
$O8b_{i48f}/O8b_{i8a}$	-11.12	-8.74	$-13.97/-9.84$
Frenkel $V_{O48f} + O8b_{i48f}$	3.52	3.42	2.22
Frenkel $V_{O8a} + O8b_{i8a}$	3.58	3.59	1.85
Split Vacancy $(2V_{O48f} + O_i)$	—	5.36	6.74

Table 6. Defect formation energies (eV/defect), corrected for two pairs of compact cation antisite defects. Frenkel energies are for isolated point defects

Defect	W&C	Bush	DOM
V_{O48f}	16.06	—	16.68
V_{O8a}	15.95	—	12.25
$O8b_{i48f}/O8b_{i8a}$	-13.32	—	$-14.54/-8.87$
Frenkel $V_{O48f} + O8b_{i48f}$	1.37	—	1.07
Frenkel $V_{O8a} + O8b_{i8a}$	1.31	—	1.69
Split Vacancy $(2V_{O48f} + O_i)$	—	6.63	6.39

cation disorder is both localized and closely associated with the anion disorder, it is reasonable to expect that many of the anion Frenkel defects may be formed by near neighbor, rather than isolated, vacancies and interstitials that occur in close proximity to the cation antisite disorder. It is therefore informative to investigate the stability of such localized Frenkel defects to determine which are more likely to occur.

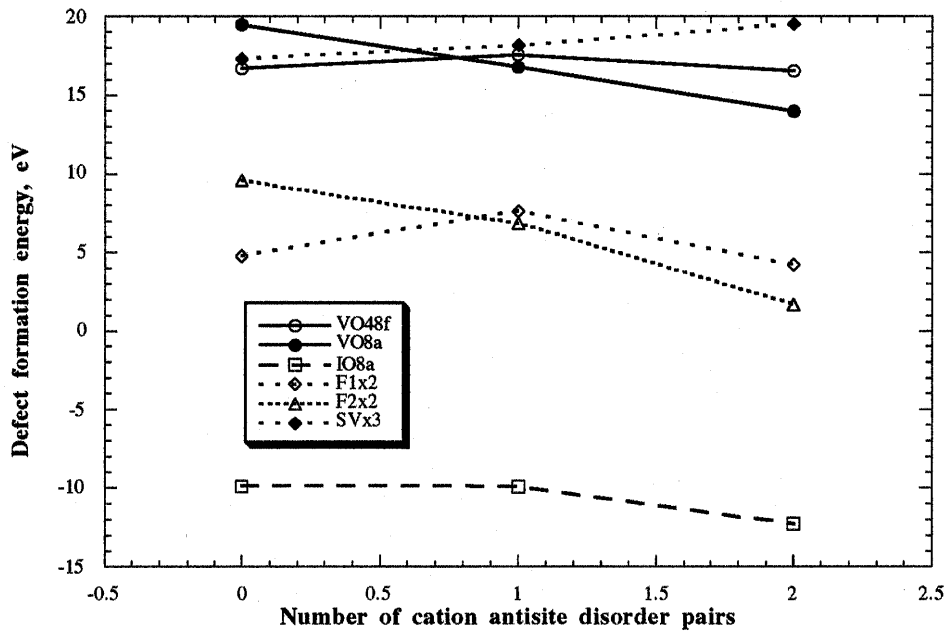Two cases of near neighbor Frenkel configurations

Fig. 4. Averaged defect formation energies for the three sets of potentials. F1 and F2 are the first and second Frenkel defects in the previous tables, respectively. SV is the split vacancy case. Each has been multiplied by the number of point defects to permit direct comparison with the simple vacancy cases.
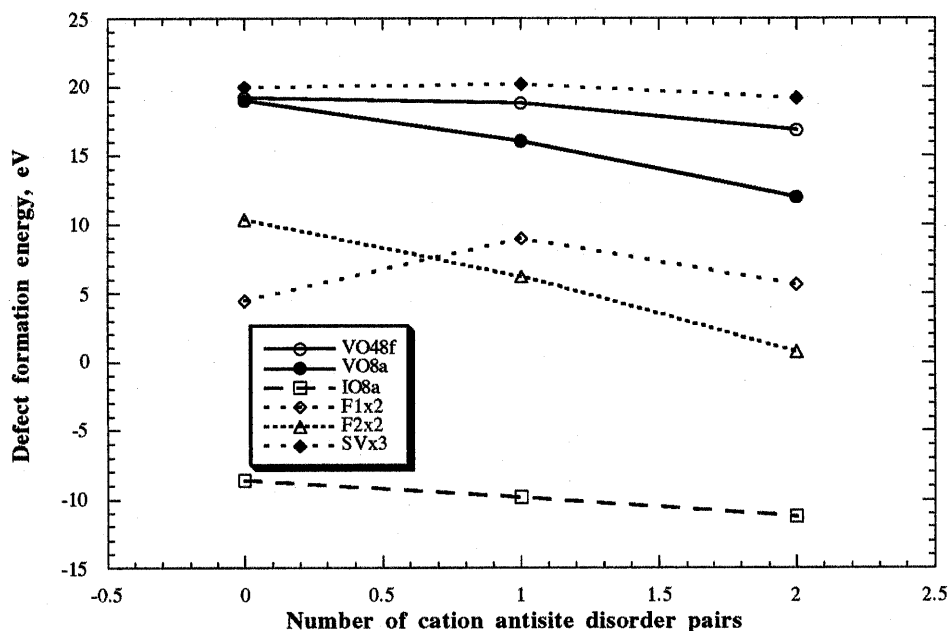
Fig. 5. Defect formation energies for the DOM potentials. F1 and F2 are the first and second Frenkel defects in the previous tables, respectively. SV is the split vacancy case. Each has been multiplied by the number of defects to permit direct comparison with the simple vacancy cases.

were simulated. The first case placed the 8b interstitial within a compact cluster of cation antisite defects, with the associated anion vacancy located at the first or second near neighbor distance from the 8b interstitial site. Vacancy-interstitial distances were 0.205 and 0.364 nm for the first and second near neighbors, respectively, for the first Frenkel, and 0.442 and 0.511 nm for the second Frenkel. The second case reversed the above configuration by placing the vacancy within the cation antisite cluster, and the 8b interstitial was placed at the first or second near neighbor position. Vacancy-interstitial distances were 0.364 and 0.596 nm for the first and second near neighbors, respectively, for the first Frenkel, and 0.442 and 0.511 nm for the second Frenkel. The results shown in Table 7 are corrected for the disorder energies. All calculations were performed using the DOM potentials with 300–315 ion cores in Region 1.

Table 7. Frenkel defect formation energies (eV) for $F1 = V_{O48f} + O8b_i$ and $F2 = V_{O8a} + O8b_i$, when the vacancy and interstitial are near neighbors. Cases 1 and 2 are for compact cation antisite disorder clustered around the interstitial and vacancy, respectively, while the associated vacancy or interstitial was located at the first or second near neighbor (nn) sites

Frenkel	Case	Disorder	1^{st}nn	2^{nd}nn
F1	1	0X	Unstable	3.04
F1	1	1X	Unstable	Unstable
F1	1	2X	Unstable	Unstable
F2	1	0X	7.99	Unstable
F2	1	1X	Unstable	Unstable
F2	1	2X	1.20	Unstable
F1	2	0X	3.34	Unstable
F1	2	1X	4.24	Unstable
F1	2	2X	Unstable	Unstable
F2	2	0X	8.26	Unstable
F2	2	1X	Unstable	Unstable
F2	2	2X	Unstable	Unstable

The large fraction (75%) of unstable defects indicates that localized Frenkels are stable only under limited conditions of compact disorder. Most of the stable Frenkels occurred for symmetric (0X or 2X) antisite disorder for nearest neighbor vacancies and interstitials. The lone stable Frenkel for asymmetric disorder (1X) has the highest formation energy for stable F1 defects. There are an equal number of stable Frenkels for antisite disorder clustered around interstitials and around vacancies (cases 1 and 2, respectively). Most of the stable Frenkels were for first, rather than second, near neighbor vacancy-interstitial pairs. This confirms the intimate connection between cation and anion disorder.

F1 defect instability was caused by the O48f interstitial filling the O48f vacancy, which involved more than the original point defects for second near neighbor vacancy-interstitial pairs. F2 instability was caused by an analogous O8a reaction for first near neighbor vacancy-interstitial pairs. F2 instability for second near neighbor pairs was caused by an O48f atom filling the 8a vacancy, thus transforming the F2 into an F1 defect. This is consistent with a low energy (0.2–0.3 eV) vacancy migration path $V_{O8a} \rightarrow V_{O48f}$ that ''enables'' or activates the dominant $V_{O48f} \rightarrow V_{O48f}$ anion conduction path in these pyrochlores, as described in the next section. The instability of all F2 defects for second near neighbors indicates that although V_{O8a} and F2 defects are easier to form, they can easily degenerate into V_{O48f} and F1 defects.

The first near neighbor F2 defect is stable for 0X disorder, but the energies are quite high, and this is unlikely to provide an important source of oxygen vacancies. However, F2 at 2X disorder for first near neighbors has a low formation energy (1.2 eV) when the interstitial is ''trapped'' by compact disorder (case 1). This is consistent with oxygen vacancy migration energetics at high disorder (next section).

Several calculations were also performed to explore a more ''open'' antisite disorder configuration, where either one or both of the Gd were at second near neighbor sites. The cation disorder was configured so as to separate the interstitial and the vacancy, forming a disorder ''barrier'' to retard recombination. One incidence of a stable F1 defect was found with a formation energy of 0.79 eV at 2X open disorder. A stable F2 was also found at 0.58 eV for this disorder. These preliminary results are close to the activation energy for oxygen vacancy migration observed experimentally in $Gd_2(Zr_{0.6}Ti_{0.4})_2O_7$ [5], and are

under further investigation. This indicates that vacancy formation could require nearly the same energy as vacancy migration, for some disorder configurations. A general observation is that the stability of near neighbor Frenkels in this material is sensitive to the configuration of the cation antisite disorder. A more exhaustive search for disorder configurations that ensure Frenkel stability is probably justified to fully understand why the ionic conductivity of the $Gd_2(Zr_xTi_{1-x})_2O_7$ pyrochlores is maximized for intermediate additions of Zr.

8. Cation Antisite Disorder and Oxygen Vacancy Migration

A total of eight O-O vacancy migration paths were investigated. When the pyrochlore structure is viewed as a collection of TiO_6 octahedra and GdO_8 dodecahedra, these paths can be described as follows. Each O48f oxygen has as neighbors four other O48f atoms at 0.265 nm, four at 0.285 nm, two at 0.389 nm and one at 0.403 nm. Jumps for the first two distances are along edges of the TiO_6 octahedra. The 0.265 nm edges are shared with the GdO_8 dodecahedra, while the 0.285 nm octahedra edges are unshared. Direct jumps for the 0.389 nm path are impossible because a Ti atom is centered between the two O48f sites. O48f-O48f jumps for the 0.403 nm distance occur across the octrahedral void centered within the four TiO_6 octahedra in Fig. 2, and pass through the 8b site. Each O48f atom also has as neighbors one O8a atom at 0.307 nm and two O8a atoms at 0.363 nm. The 0.307 nm paths are shared edges between dodecahedra, while the 0.363 nm paths define unshared dodecahedron edges. The oxygen vacancy migration paths treated are shown in Tables 8, 9 and 10. Jumps between 8a sites were not considered because the shortest path has a Gd atom exactly between the two 8a sites, and the other 8a-8a path was very long (0.7 nm). The two entries for the 0.285 nm paths were for oxygen migration parallel to and normal to the ⟨110⟩ Gd rows in Fig. 3, and are denoted ∥ and ⊥ respectively.

For computational expediency, these calculations were performed with 100–150 ion cores in Region 1. The saddle point energies for each case were computed with the disorder present. The corresponding vacancy formation energies (also including the disorder) were subtracted from the saddle point

energies to give the migration activation energies in Tables 8, 9, and 10. For cases of migration between two distinct sites (48f vs. 8a), care was taken to subtract the proper vacancy energy from the saddle point energy. Whether atom migration or vacancy migration is considered, the correct vacancy energy to subtract is that of the initial rather than the final site. For example, during vacancy migration from site A (initial) to site B (final), an atom with site B properties migrates from B to A, and the initial vacancy energy is that of site A. Notations such as $V_{O48f} \rightarrow V_{O8a}$ in Tables 8–10 indicate the vacancy migration direction, rather than ion migration.

The scatter in results between the three potential sets is again evident in Tables 8–10. It is again advantageous to average over the potentials for each migration path, which gives the results shown in Fig. 6. This figure exhibits several interesting features. The first is that the migration path energies appear to separate into two groups. The group with higher energies (filled symbols) is composed of the longer paths (0.285 ∥, 0.363, and 0.403 nm) which are not shared between polyhedra. The group with lower energies (open symbols) is composed of shorter paths, of which the 0.265 and 0.307 nm cases are shared polyhedra edges and the 0.285 ∣−nm path is

Table 8. Oxygen vacancy migration energies (eV), with no cation disorder. Notations such as $V_{O48f} \rightarrow V_{O8a}$ indicate the vacancy migration direction, rather than ion migration

Ion	Dist., nm	Description	W&C	Bush	DOM
O48f	0.265	TiO_6 oct. edge	0.33	0.04	0.24
O48f	0.285	TiO_6 oct. edge (∥)	0.67	1.02	0.80
O48f	0.285	TiO_6 oct. edge (∣−)	0.67	1.02	0.80
O48f	0.307	$V_{O8a} \rightarrow V_{O48f}$	0.36	0.15	0.33
O8a	0.307	$V_{O48f} \rightarrow V_{O8a}$	3.81	5.27	4.26
O48f	0.363	$V_{O8a} \rightarrow V_{O48f}$	2.57	2.40	2.91
O8a	0.363	$V_{O48f} \rightarrow V_{O8a}$	6.03	7.54	6.48
O48f	0.403	TiO_6 oct. void (8b)	2.89	4.11	3.31

Table 9. Oxygen vacancy migration energies (eV) corrected for one pair of compact cation antisite defects. Notations such as $V_{O48f} \rightarrow V_{O8a}$ indicate the vacancy migration direction, rather than ion migration

Ion	Dist., nm	Description	W&C	Bush	DOM
O48f	0.265	TiO_6 oct. edge	0.26	0.74	2.12
O48f	0.285	TiO_6 oct. edge (∥)	2.44	2.85	1.30
O48f	0.285	TiO_6 oct. edge (∣−)	0.78	0.30	0.47
O48f	0.307	$V_{O8a} \rightarrow V_{O48f}$	0.67	2.60	1.24
O8a	0.307	$V_{O48f} \rightarrow V_{O8a}$	0.79	2.94	2.10
O48f	0.363	$V_{O8a} \rightarrow V_{O48f}$	5.82	0.26	1.09
O8a	0.363	$V_{O48f} \rightarrow V_{O8a}$	5.94	0.60	5.80
O48f	0.403	TiO_6 oct. void (8b)	2.61	4.02	2.61

Table 10. Oxygen vacancy migration energies (eV) corrected for two pairs of compact cation antisite defects. Notations such as $V_{O48f} \rightarrow V_{O8a}$ indicate the vacancy migration direction, rather than ion migration

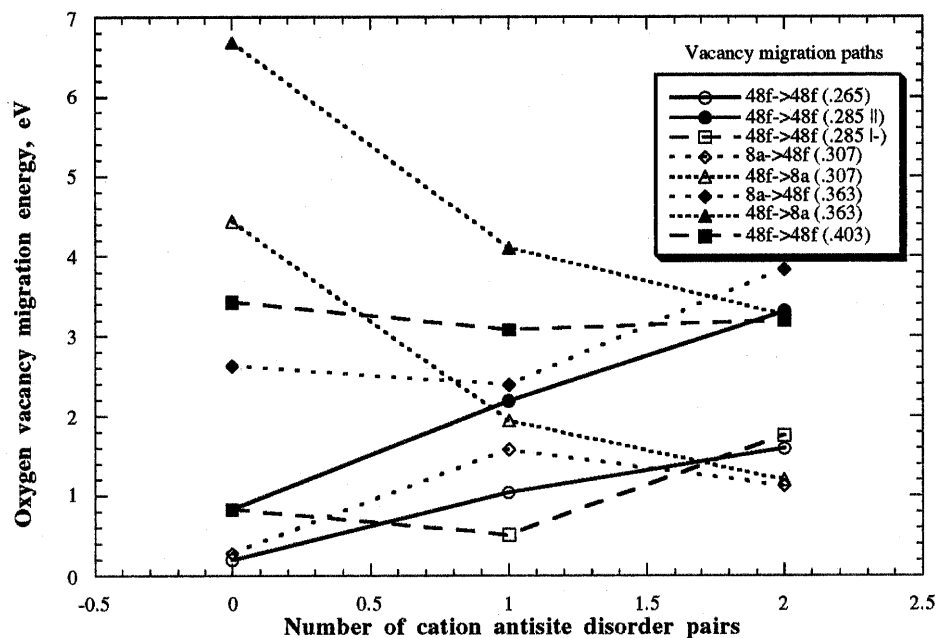| Ion	Dist., nm	Description	W&C	Bush	DOM
O48f	0.265	TiO_6 oct. edge	2.56	0.30	1.92
O48f	0.285	TiO_6 oct. edge (∥)	3.32	3.31	—
O48f	0.285	TiO_6 oct. edge (∣−)	1.89	1.99	1.41
O48f	0.307	$V_{O8a} \rightarrow V_{O48f}$	0.49	0.79	2.13
O8a	0.307	$V_{O48f} \rightarrow V_{O8a}$	0.38	1.15	2.07
O48f	0.363	$V_{O8a} \rightarrow V_{O48f}$	5.05	2.44	4.04
O8a	0.363	$V_{O48f} \rightarrow V_{O8a}$	4.94	2.80	2.04
O48f	0.403	TiO_6 oct. void (8b)	2.70	4.60	2.30

Fig. 6. Oxygen vacancy migration energies averaged over three potentials for compact disorder.

unshared. A second interesting feature is that each curve appears to have a "brother" in the other group, indicated by the matching line types. For the most part, the shapes of the corresponding brothers are qualitatively similar. A third interesting feature of Fig. 6 is that the members of each group appear to converge towards a nearly common migration energy as the cation disorder increases. This behavior is more clearly exhibited in Fig. 7. The convergence of both groups to a common energy is to be expected, because each oxygen specie is approaching the same cation charge environment ($+14$ |e|) as the disorder increases. The improved representation of this effect by the DOM potentials supports the validity of these potentials.

The most probable oxygen vacancy migration paths and energies can be deduced from Figs. 6 and 7. For no cation disorder, the dominant migration path is between 48f sites along the shortest (0.265 nm) shared edges of the TiO_6 octahedra, and requires an average activation energy of about 0.2 eV. This is in good agreement with the results (0.18 eV) of Wilde and Catlow [8,9], who used this result to suggest that vacancy formation could be more important than migration energetics. Empty 8a sites can be filled by 48f oxygens at an expense of 0.28 eV, thus enabling migration within the

0.265 nm 48f oxygen sublattice shown in Fig. 8. This migration network is three dimensional, so oxygen vacancy migration is expected to be isotropic in $Gd_2Ti_2O_7$. At 1X cation disorder, the lowest migration energy is for the 0.285 I$-$ nm path that is roughly normal to the Gd rows in Fig. 3. However, this is not a connected network, as can be seen in Fig. 1. Therefore, vacancy migration is again dominated by the 48f sites along the 0.265 nm paths, with an average energy of 1.02 eV. At 2X cation disorder, the lowest migration energy is for the 48f atoms to fill empty 8a sites along the 0.307 nm path, at an averaged energy expense of 1.13 eV. This also is not a connected network, and the 0.265 nm 48f-48f paths dominate at an averaged energy of 1.59 eV.

The above simulations were of relatively low accuracy, with 100–150 ion cores in Region 1, and were intended as scoping calculations to reveal the most important trends in $Gd_2Ti_2O_7$ oxygen vacancy migration mechanisms. Two such trends are of note. The first is that the migration energies in the well known (0.265 nm) 48f–48f path increase as compact disorder increases. This is opposite of the trends found by Wilde and Catlow [9] for the zirconate using molecular dynamics techniques. The second important trend is that oxygen vacancy migration between 8a and 48f sites also has relatively low energy
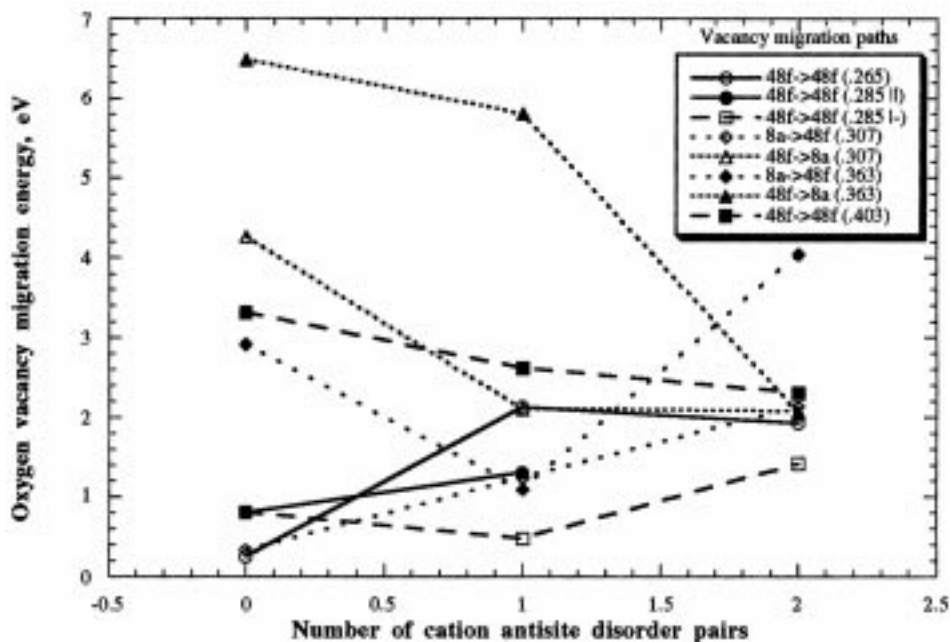
Fig. 7. Oxygen vacancy migration energies for the DOM potentials for compact disorder.

requirements. Additional calculations were performed to explore these trends further, as follows.

The DOM potentials were refined so that they also treated the zirconate. Simultaneously fitting the potentials to the structures, elastic constants, and dielectric properties of $Gd_2(Zr_xTi_{1-x})_2O_7$ for $x = 0.0$, 0.6 and 1.0, while holding the Gd-O and O-O potentials constant, resulted in only small changes to
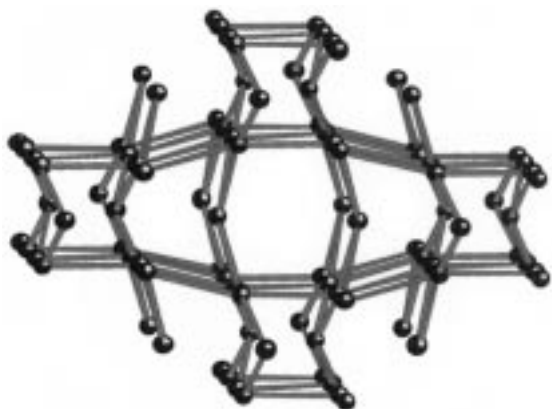

Fig. 8. Three dimensional network of the oxygen migration paths along the shared, 0.265 nm TiO_6 octahedra edges of a $2 \times 2 \times 2$ supercell. Spheres are O48f atoms. Viewed along $\langle 110 \rangle$.

the Ti-O potential and the oxygen charges. The refined potential parameters were within a few percent of the values given in Table 1, with the exception of the O48f spring constant, which increased to $412.6 \, eV/\mathring{A}^6$. Table 11 shows the results of preliminary calculations (100–150 ion cores in Region 1) for ''open'' disorder, as described above. In this instance, the cation antisite defects were oriented pointing away from the ends of the oxygen vacancy migration path, rather than tightly clustered around the path [11]. This in essence allowed for polarization of the cation-anion defect cluster, where the cation defects were juxtaposed to the anion defects. Only the three most important migration paths from Figs. 6 and 7 were investigated in Table 11, where the energetically preferred values are shown in bold print. The bold entries were further refined using 300–315 ion cores in Region 1, giving migration energies of 0.60, 0.23, and 0.14 eV for the $V_{O48f} \rightarrow V_{O48f}$, $V_{O8a} \rightarrow V_{O48f}$, and $V_{O48f} \rightarrow V_{O8a}$ paths, respectively. These are discussed in more detail in the following paragraphs.

The $V_{O48f} \rightarrow V_{O48f}$ path is easiest when the vacancy moves towards moderate (1X) open disorder, apparently to relieve local stresses there. The migration energy of 0.60 eV is consistent with experimentally determined values of $\sim 0.8 \, eV$ for

Table 11. Oxygen vacancy migration energies (eV) for ''open'' disorder allowing polarization of defect clusters

Disorder	Description	$V_{O48f} \rightarrow V_{O48f}$	$V_{O8a} \rightarrow V_{O48f}$	$V_{O48f} \rightarrow V_{O8a}$
0X	Ordered	1.17	**0.23**	4.19
1X	Towards disorder	**0.63**	3.20	3.88
1X	Away from disorder	1.76	3.26	1.80
2X	High disorder	3.00	2.68	**0.35**

$Gd_2(Zr_{0.6}Ti_{0.4})_2O_7$ [1,2,4,5]. This result is also consistent with the stability of the F1 Frenkel for 1X disorder (case 2) in Table 7, since an O48f vacancy must exist for this path to be active.

The $V_{O8a} \rightarrow V_{O48f}$ path is easiest for the ordered material. This result is consistent with the stability of the F1 Frenkel at 0X disorder (both cases) in Table 7. It is also consistent with the instability of the F2 Frenkels at 0X (second near neighbors) in Table 7, which was caused by 8a vacancy migration to 48f sites. This mechanism for depositing a vacancy on the 48f sublattice provides a low energy (0.23 eV) mechanism to enable the 48f-48f migration path that is primarily responsible for ionic conduction.

The $V_{O48f} \rightarrow V_{O8a}$ path is easiest for high (2X) disorder. This result is consistent with the stability of the F2 Frenkel at 2X disorder (case 1) in Table 7, via transfer of an oxygen vacancy from the 48f sublattice to the 8a sublattice at 0.14 eV. The migration energy decreased to a very small value for the zirconate [11], indicating the existence of a mechanism for retarding ionic conductivity at excessive local disorder (2X).

Two general observations are now possible: (1) Comparing the results in Table 11 to those in Tables 8–10 demonstrates the sensitivity of oxygen vacancy migration to the configuration of the antisite disorder. (2) The 8a oxygens appear to be involved in ionic conduction by providing low energy mechanisms for first enabling the 48f migration network at low disorder, and then disabling the same network at high disorder.

9.   Discussion and Conclusions

This section is roughly divided into discussions of the computational methods and the results. The energy minimization, Mott-Littleton, and shell model methods used in this work have a long history of success for defect studies in ionic materials, so that further discussion is not necessary. Two primary sources of uncertainty were inherent in this work: the rather small Mott-Littleton Region 1 radius employed for the scoping calculations, and the differences between the potential sets. The general effects of increasing R1 are well known (e.g., [31]), and we have used such larger values where appropriate to obtain more accurate results.

The uncertainties originating from the differences in the three sets of potentials reflect some of the caveats to be considered when working with empirical potentials. However, consistency of results seemed to be improved by either averaging or by using the DOM potentials. The DOM potentials employed distinct core-shell parameters (charges and spring constants) for the two crystallographically distinct oxygens (48f vs. 8a) in the pyrochlore, so that aspects of both other sets of potentials were incorporated. In essence, the differences in polarizabilities of the oxygens at the two distinct sites were modeled beyond the simple effect of short range damping. This is unique to the study of these pyrochlores. To our knowledge, the use of this ''distinct oxygen model'' to determine the directional anisotropy for oxygen vacancy migrations is also a unique application for the energy minimization method.

The distinct oxygen model also requires that another important caveat be realized. This is basically an ''end state'' calculation, and is an approximation of the changes in effective charge and polarization that occur when an oxygen atom moves from one site to another. It is valid as long as the migrating atom does not approach too closely to a site for which its shell properties do not apply. The end state approximation could be questioned for cases of compact high disorder, where the cationic charge environment of all oxygen sites is the same. However, this question may not apply for the more dilute disorder characteristic of optimized ionic conductivity. This can be demonstrated as follows. Eight formula units per unit cell gives 16 cation pairs in a box about 1 nm on a side. At optimum ionic conductivity (60% Zr), about 10% of these cation

pairs are disordered, giving two disordered pairs per unit cell. Assuming that such pairs form spherical disorder regions with diameters approximately twice the smallest cation-cation distance $(2 \times 0.365\,\text{nm})$, these two regions can readily be arranged in a unit cell without overlapping. Consequently, the disorder is ''localized'', and corresponds to the 1X disorder used herein. However, at 100% Zr about 35% of the cation pairs are disordered, giving five to six local disorder regions in the unit cell, which can overlap and produce local 2X disorder regions. The result is that the end state approximation is valid at least for the most important range of Zr content, where ionic conductivity is maximized.

The above argument leads to a description of a likely mechanism for long range ionic conduction in $Gd_2(Zr_xTi_{1-x})_2O_7$, as follows. For $x = 0$, oxygen vacancy migration is limited by the energy of the $V_{O48f} \rightarrow V_{O48f}$ path at 0X (1.17 eV, Table 11) because cation antisite disorder is dilute and very localized. The most frequent vacancies (V_{O8a}) may be fed into the 48f network at low energies (0.23 eV from Table 11). For $x = 0.6$, 1X disorder regions are still rather localized, so the same 48f path dominates in ordered regions (0.79 eV from Table 3 of [11]). For $x = 1.0$, 1X disorder may dominate the $V_{O48f} \rightarrow V_{O48f}$ path (0.59 eV from Table 3 of [11]), but 2X disorder regions also occur. The apparent activation energy for oxygen migration may be increased as 2X disorder regions ''absorb'' some of the oxygen vacancies from the 48f network, necessitating generation of additional 48f vacancies at higher energy expense.

General conclusions that can be drawn from this work are:

- Anion defect formation and migration energetics are sensitive to the amount and configuration of the cation antisite disorder.
- Regions of local order and regions of local disorder are probably both needed to explain the observed ionic conduction behavior. This is consistent with the expectation of relatively dilute cation antisite disorder in the material at optimum ionic conductivity.
- In the vicinity of cation antisite disorder, most of the stable Frenkels were for first, rather than second, near neighbor vacancy-interstitial pairs. This confirmed the intimate connection between cation and anion disorder.

- The 48f oxygen sublattice controls ion migration, but the 8a oxygen sublattice is involved in enabling the migration at low disorder and disabling the migration at high disorder.

Acknowledgments

References

1. M. Spears, S. Kramer, H.L. Tuller, and P.K. Moon, in *Proc. 1st Int'l. Symp. on Ionic and Mixed Conducting Ceramics*, edited by T.A. Ramanarayan and H.L. Tuller (Materials Research Society, Pittsburgh, 1991), p. 32.
2. P.K. Moon and H.L. Tuller, *Sensors and Actuators*, **B1**, 199 (1990).
3. W.J. Weber, et al., *J. Mater. Res.*, **13**, 1434 (1998).
4. H.L. Tuller, *Solid State Ionics*, **52**, 135 (1992).
5. P.K. Moon and H.L. Tuller, in *Solid State Ionics, Proc. Symp.* **135**, edited by G. Nazri, R.A. Huggins, D.F. Shriver (Materials Research Society, Pittsburgh, 1990), p. 149.
6. S.M. Haile, B.J. Wuensch, and E. Prince, in *Neutron Scattering for Materials Science, Proc. Symp.* **166**, edited by S.M. Shapiro, S.C. Moss, J.D. Jorgensen (Materials Research Society, Pittsburgh, 1990), p. 81.
7. M.P. van Dijk, A.N. Cormack, A.J. Burgraaf, and C.R.A. Catlow, *Solid State Ionics*, **17**, 159 (1985).
8. P.J. Wilde and C.R.A. Catlow, in *Ionic and Mixed Conducting Ceramics*, edited by T.A. Ramanarayanan and H.L. Tuller (Electrochem. Soc. Proceedings 91-12, 1991), p. 18.
9. P.J. Wilde and C.R.A. Catlow, *Solid State Ionics*, **112**, 173 (1998).
10. P.J. Wilde and C.R.A. Catlow, *Solid State Ionics*, **112**, 185 (1998).
11. R.E. Williford, W.J. Weber, R. Devanathan, and J.D. Gale, in *Materials Res. Symp. Proc. 538, Multiscale Modeling of Materials,* (Materials Research Society, Pittsburgh, 1998), p. 235.
12. H. Nyman, S. Andersson, B.G. Hyde, and M. O'Keeffe, *J. Sol. State Chem.*, **26**, 123 (1978).
13. O. Knop, F. Brisse, and L. Castelliz, *Can. J. Chem.*, **46**(6), 971 (1969).
14. M.A. Subramanian and A.W. Sleight, in *Handbook on the Physics and Chemistry of Rare Earths*, **16**, Chapter 107, edited by K.A. Gschneider and L. Eyring, (Elsevier Science Publ BV, Amsterdam, 1993), p. 225.
15. W.W. Barker, J. Graham, O. Knop, and F. Brisse, in *The Chemistry of Extended Defects in Non-metallic Solids,*

Proceedings of Inst. for Adv. Study, edited by L.R. Eyring and M. O'Keeffe (North-Holland Publ., 1969), p. 198.

16. G. Albanese, A. Deriu, J.E. Greedan, M.S. Seehra, K. Siratori, and H.P.J. Wijn, in *Properties on Non-Metallic Inorganic Compounds Based on Transition Elements, Vol. 27 of Landolt-Borstein, Group III: Crystal and solid State Physics*, edited by H.P.J. Wijn (Springer-Verlag, Heidelberg, 1992), p. 100.

17. N.T. Vandenborre, E. Husson, and H. Brusset, *Spectrochem. Acta*, **37A**, 113 (1981).

18. M. Queslati, M. Balkanski, P.K. Moon, and H.L. Tuller, in *Materials Res. Symp. Proc.* **135**, (Materials Research Society, Pittsburgh, 1989), p. 199.

19. J.D. Gale, *J. Chem. Soc., Faraday Trans.*, **93**, 629 (1997).

20. J.D. Gale, *Phil. Mag. B*, **73**, 3 (1996).

21. N.F. Mott and M.J. Littleton, *Trans. Faraday Soc.*, **34**, 485 (1938).

22. W. Hayes and A.M. Stoneham, *Defects and defect processes in nonmetallic solids* (John Wiley & Sons, New York, 1985).

23. B.G. Dick and A.W. Overhauser, *Phys. Rev.*, **112**, 90 (1958).

24. T.S. Bush, J.D. Gale, C.R.A. Catlow, and P.D. Battle, *J. Mater. Chem.*, **4**, 831 (1994).

25. C.R.A. Catlow, *Proc. Royal Soc. A*, **333**, 533 (1977).

26. P.W. Fowler, *Molec. Simul.*, **4**, 313 (1990).

27. G.V. Lewis and C.R.A. Catlow, *J. Phys. C: Sol. State Phys.*, **18**, 1149 (1985).

28. M.J.L. Sangster and A.M. Stoneham, *Phil. Mag.*, **43**, 597 (1980).

29. A. Dietrich, *Molec. Simul.*, **11**(5), 251 (1992).

30. L.H. Brixner, *Inorganic Chem.*, **3**, 1065 (1964).

31. P.W.M. Jacobs and E.A. Kotomin, *Phil. Mag. A*, **68**, 695 (1993).